Dynamic Mapping of Electrochemiluminescence Reactivity in Space: Application to Bead-Based Assays

Dongni Han, Danjun Fang, Giovanni Valenti, Francesco Paolucci, Frédéric Kanoufi, Dechen Jiang, Neso Sojic

Dynamic Mapping of Electrochemiluminescence Reactivity in Space: Application to Bead-Based Assays

Dongni Han, Danjun Fang, Giovanni Valenti, Francesco Paolucci, Frédéric Kanoufi, Dechen Jiang,* and Neso Sojic*

ABSTRACT: As an electrochemical technique offering an optical readout, electrochemiluminescence (ECL) evolved recently into a powerful microscopy technique with the visualization of a wide range of microscopic entities. However, the dynamic imaging of transient ECL events did not receive intensive attention due to the limited number of electrogenerated photons. Here, the reaction kinetics of the model ECL bioassay system was revealed by dynamic imaging of single $[Ru(bpy)_3]^{2+}$-functionalized beads in the presence of the efficient tripropylamine coreactant. The time profile behavior of ECL emission, the variations of the ECL layer thickness, and the position of maximum ECL intensity over time were investigated, which were not achieved by static imaging in previous studies. Moreover, the dynamics of the ECL emission were confronted with the simulation. The reported dynamic ECL imaging allows the investigation of the ECL kinetics and mechanisms operating in bioassays and cell microscopy.

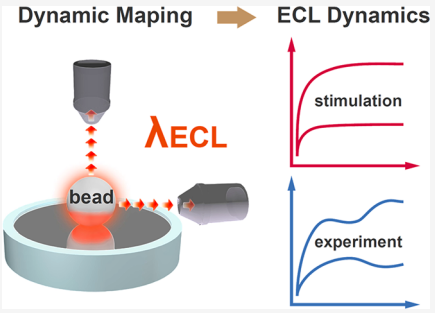

INTRODUCTION

After decades of fundamental research, electrochemiluminescence (ECL) is an analytical technique that has gained popularity in many fields, including imaging and biosensing.[1−6] The latter has led to successful commercial instruments for biomarker detection.[7−10] ECL is a luminescent phenomenon that is triggered by electrochemical excitation, and the signals are the current and the photons generated. Since it gives an optical readout, the spatial distribution of this signal can be mapped easily and offers the opportunity to perform microscopy experiments.[3,4,11−14] Given the high sensitivity and spatiotemporal controllability of ECL,[12,15,16] the combination between ECL and imaging enables the visualization of a variety of microscopic objects and cells.[8,15,17−26] ECL generation itself is a dynamic electrochemical process that integrates many elementary steps: the initial electrochemical reactions at the electrode surface, the exergonic electron-transfer reactions populating the excited state of the luminophore, and finally its radiative relaxation to the ground state with the light emission. Most of the ECL imaging works study and visualize static entities such as micro/nanoparticles, cells, or organelles and require long exposure time of the 2D photodetector (typically, a CCD camera).[27−36] Indeed, a few seconds or tens of seconds are classically used to accumulate enough photons in order to obtain a clear image of the analyzed objects.[4,37−40] This is due to the low number of generated photons during the ECL process and to the limited ECL efficiency of the luminophores.[14] This limitation implies that dynamic processes in the subsecond or millisecond timescales are rarely investigated by ECL.[4,41,42] For example, Zhu and co-workers imaged the collisions of single $[Ru(bpy)_3]^{2+}$-doped silica nanoparticles by ECL with a 0.2 s exposure time.[41] Feng and co-workers reported the imaging of single ECL photons with an exposure time of 0.51 ms.[4] However, they needed 150 s to obtain an ECL image of a cell. Therefore, a clear need exists for the development of ECL microscopy with improved dynamics.

Thus, we report herein the dynamic ECL imaging of single $[Ru(bpy)_3]^{2+}$-functionalized microbeads. Such beads are widely used for ECL-based immunoassays and are successfully commercialized for the diagnostics. It is a very active area with different research facets, ranging from the synthesis of brighter ECL labels, to the deciphering of the mechanistic pathways, and to the development of original bioassay strategies.[8,9,17,21,43−47] As a matter of fact, some of us previously reported a preliminary example of dynamic ECL imaging investigation of dye-doped silica nanoparticles anchored onto beads aimed at evaluating the improving effect on the emission signal stability associated with the silica matrix in which the luminophores are embedded.[45]

The $[Ru(bpy)_3]^{2+}$ luminophore with the sacrificial tripropylamine (TPA) coreactant forms a classical ECL system, which is the basis of a majority of immunoassays and DNA analysis.[48,49]

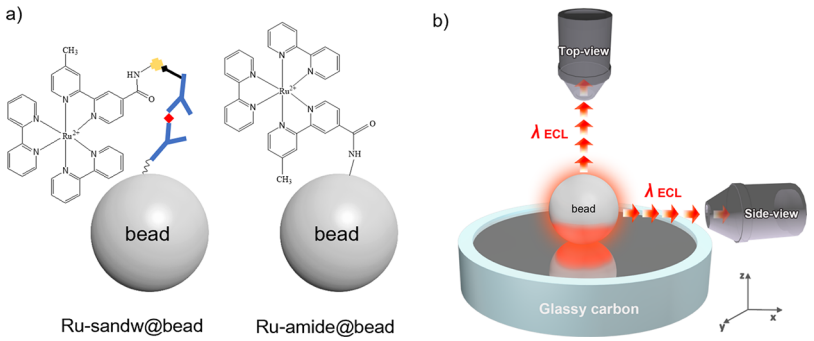

Figure 1. (a) Polystyrene bead functionalized with the ECL label by sandwich immunoassay (left) or an amide covalent bond (right). (b) Scheme of the optical configurations used for dynamic ECL imaging of a single labeled bead under the microscope: top view and side view.

In commercial ECL assays, $[Ru(bpy)_3]^{2+}$-labeled analytes are immobilized on magnetic microbeads that are attracted to the working electrode by a magnetic field. ECL emission is generated by imposing an anodic potential with the irreversible oxidation of TPA.[50] The "revisited route" proposed by Miao et al. involves the generation of the $[Ru(bpy)_3]^{2+}$ excited state, which is obtained by the electron-transfer reactions with the electrogenerated TPA radicals (i.e., without the direct oxidation of $[Ru(bpy)_3]^{2+}$ at the electrode surface).[48] This mechanistic pathway describes mainly bead-based ECL emission (vide infra). It is the predominant process for ECL emission within the diffusion distance of TPA radicals (about 3−4 μm).[29,51] Mapping the ECL reactivity allowed to record the ECL behavior in 3D mode, to propose new reaction mechanisms, and simultaneously to study the complexity of the ECL mechanisms involving radicals with short lifetimes.[8,9,17,21,49,52,53] As already mentioned, the research on ECL imaging has mainly focused on static imaging. However, with the uncovering of the complex kinetics in ECL reactions, static imaging has limited the description of those fast and tiny changes. Dynamic imaging of the ECL processes has become a challenging task.

In this work, we performed dynamic imaging of the ECL reactivity in space to investigate the kinetics of the $[Ru(bpy)_3]^{2+}$/TPA system at the single-bead level. The $[Ru(bpy)_3]^{2+}$ labels were attached to the microbead surface via a sandwich immunoassay or amide covalent bond (Figure 1a). In this way, the immobilized $[Ru(bpy)_3]^{2+}$ centers are exposed to the electrogenerated TPA radicals. Top-view and side-view configurations (Figure 1b) enable the optical signals to be collected in 3D mode with short exposure times (50 and 100 ms). Dynamic variations of the ECL emission layer and instant ECL intensity on the single beads were recorded, providing kinetic information for the underlying electrochemical reactions. In comparison to the simulation, factors influencing the kinetics of ECL in the experimental conditions were found, which could support the optimization of ECL immunoassays.

EXPERIMENTAL SECTION

Reagents. All the reagents were purchased from Sigma-Aldrich unless otherwise noted. Polystyrene (PS) beads (diameter: 12 μm) were obtained from Kisker Biotech GmbH & Co. Capture antibody specific for interleukin 8 (IL-8), the complementary biotinylated detection antibody, and IL-8 recombinant protein were obtained from R&D Systems Inc. TBS StartingBlock, PBS StartingBlock, and PBS Protein-Free blocking buffers were obtained from Pierce Biotechnology Inc. The streptavidin-modified $[Ru(bpy)_3]^{2+}$ complex used as an ECL label in the immunoassay experiments was synthesized according to the procedure reported previously.[47]

Instrumentation. The electrochemical cell was a three-electrode system: a working glassy carbon (GC) electrode, a platinum wire as the counter electrode, and Ag/AgCl/KCl (3 M) electrode as the reference electrode. The experiments were performed by using a μ-Autolab type III potentiostat. The PL and ECL images were recorded using an epifluorescence microscope from Leica (DMI6000, Leica Microsystems) and an electron-multiplying charge-coupled device (EM-CCD 9100-13) camera from Hamamatsu. PL and ECL experiments were performed in PBS containing 100 mM TPA (pH 7.4).

Immunoassay with PS Beads. The PS beads were labeled with the $[Ru(bpy)_3]^{2+}$ complex either by a sandwich immunoassay or by a peptidic bond. In the first case, antigen storage aliquots were prepared in PBS 1×/BSA 0.1%, and detection antibody storage aliquots were prepared in tris-buffered saline (TBS StartingBlock). Each washing step was done in 100 μL of TBS with 1% Tween 20. The assay was performed by incubating for 2 h the microbeads functionalized with a capture antibody (anti-IL-8) first in a sample containing an antigen (diluted to the appropriate concentration with PBS Starting Block) and washed. Then, they were incubated for 30 min in 50 μL of the biotinylated detection antibody solution (3 μg/mL of antibody in PBS StartingBlock) and washed. Finally, the ECL label was attached to form an immunocomplex by exposing the beads to a solution containing a streptavidin-modified $[Ru(bpy)_3]^{2+}$ label.

Modification of the Beads with the Amide Bond. The surface of the PS beads beared $-NH_2$ groups which allow further functionalization with the ECL $[Ru(bpy)_3]^{2+}$ label. 10 μL of bead suspension (2.5%) was washed with PBS (pH 7.4) and resuspended in 1 mL of PBS. At the same time, 1 mg of $[Ru(bpy)_3]^{2+}$-NHS ester (bis(2,2′-bipyridine)-4′-methyl-4-carboxybipyridine-ruthenium *N*-succinimidyl ester-bis-(hexafluorophosphate) was dissolved in 100 μL of dimethyl sulfoxide, and this solution was added to the bead suspension. This mixture was incubated at +4 °C for 3 h with continuous stirring. After the incubation, the beads were washed from the reaction solution with PBS 10 times by centrifugation for 10 min at 10,000 rpm to separate the beads from the solution. Finally, the beads were suspended in 1 mL of PBS and kept at 4 °C.

PL Epifluorescence Microscopy. The photoluminescence (PL) experiments have been performed in the epifluorescence mode: light from a LED was passed through an excitation filter (470 ± 20 nm), and the selected wavelength was reflected at

90° by a 505 nm dichroic mirror. Excitation light was transmitted through the objective and generated PL emission labels. A fraction of the emitted PL light is collected by the same microscope objective and transmitted through the dichroic mirror. Sample emission was filtered by a long-pass filter (515 nm) to ensure that only $[Ru(bpy)_3]^{2+}$ PL was observed. The PL images were acquired by a charge-coupled device (CCD) camera. All of the images were false color-coded. PL and ECL are shown in green and red-orange colors to differentiate PL from ECL. However, PL and ECL of the ruthenium labels generate the same emission wavelength.

RESULTS AND DISCUSSION

We selected polystyrene (PS) beads with a diameter of 12 μm as the carrier of $[Ru(bpy)_3]^{2+}$ labels to record ECL images with good spatial resolution. The $[Ru(bpy)_3]^{2+}$ label decorates the bead using two functionalization procedures (Figure 1a). The first one is the sandwich immunoassay, in which the bead is modified with the capture antibody, the antigen, the biotinylated detection antibody, and the streptavidin-modified $[Ru(bpy)_3]^{2+}$ label sequentially by specific recognition. The second procedure is the direct binding of the amino-functionalized bead and the $[Ru(bpy)_3]^{2+}$ label through an amide covalent bond. The $[Ru(bpy)_3]^{2+}$-modified beads were deposited on a glassy carbon electrode, where a constant voltage of 1.4 V was applied. We selected this anodic potential because it generates strong and stable ECL intensity (Figure S1) as it is in the region where TPA oxidation is mass-transfer-controlled. The microscope setup records ECL images of the bead from the top-view and side-view configurations for dynamic analysis (Figure 1b). Since the beads modified by both labeling procedures showed similar photoluminescence (PL) and ECL behaviors, we kept the amide-modified beads in subsequent experiments to simplify the functionalization steps.

The PL image in the top-view configuration indicates the location of the labeled bead on the electrode. The distribution of the PL intensity shows the uniform $[Ru(bpy)_3]^{2+}$ decoration on the bead surface (Figure 2a). The high PL intensity at the bead edge is caused by the reflection of the optical signal inside the PS bead with a high refractive index. To capture the full process of the ECL behavior, a continuous recording of ECL images was started a few seconds before electrical stimulation. Video S1 records the dynamic ECL behavior of a single bead. As illustrated by Figure 2b–i, the ECL intensity of each frame increased with time in the first 2 s. At t = 0.1 s, the ECL image does not reveal a clear spatial distribution due to weak emission (Figure 2b). It means that, in 0.1 s, a part of $[Ru(bpy)_3]^{2+}$ labels has been converted into the excited state and emits light signals that are enough to be captured by the recording system. However, at this time, the optical signals are still diffuse. The immobilized $[Ru(bpy)_3]^{2+}$ labels randomly react with the electrogenerated TPA radicals (TPA· and TPA·$^+$), leading to the formation of the excited state and in fine dispersive light signals. Beyond t = 0.2 s, the flux of generated ECL photons is more important, and the ECL images reveal the shape of a circled dot (Figure 2c–i). The ECL pattern consists of a ring and a central spot. To quantify these varieties, a region of interest (ROI) along the x-axis on the bead was selected for extracting the ECL profile in each frame (Figure 2c). In fact, ECL intensity increased by two- to threefold from 0.2 to 2 s (Figure 3a). During this period, the ECL signal maintained the circled dot shape. In the top-view imaging, we can consider in the first-order approximation that the central spot of ECL emission is formed by the overlay of the original light at the bottom part of the bead and the effects of the bead acting as a lens,[49] while the annular light band at the edge results from the complex optical paths in the bead. One can see that globally, the same ECL pattern is maintained over time but with a progressive increase. The variation of the height of the ECL emission layer (h_{ECL}) along the z-axis was calculated by extracting the diameter of the central spot over time (Figure S2). The value of h_{ECL} increased very rapidly in the first 0.2 s from 0.45 μm at t = 0.1 s to 1.6 at t = 0.2 s, reaching a quasi-plateau of 1.75 ± 0.34 μm for times longer than 0.2 s (Figure S3). This behavior implies that the ECL emission has complex dynamic changes over time (vide infra), which are hidden in conventional long-exposure static imaging.

We further quantified the kinetics of the ECL process by monitoring the time evolution of the ECL mean intensity (I_{ECL}) from a single $[Ru(bpy)_3]^{2+}$-decorated bead recorded with an exposure time of 100 ms (Figure 3b,c). The value of instantaneous I_{ECL} exhibited qualitatively four main phases: (i) a rapid ascent in the first 0.2 s; (ii) a slower increase; (iii) a progressive inversion of the slope; and (iv) a slow decrease of the ECL emission. The first phase (i) is very short and last for ~0.2 s. It is clearly visible when zoomed-in in the first second of the process (Figure 3c). We checked that the duration of this phase was not convoluted by the exposure time of the EMCCD. For that, we repeated the experiments with a shorter exposure time of 50 ms. The same pattern was obtained for both exposure times. As expected, the ECL mean intensity was twice as low with an exposure time of 50 ms in comparison to 100 ms (Figure 3b,c). After this first phase, from approximately 0.2 to 3–4 s, the ECL emission continues to increase but with a lower slope. Then, it reaches a quasi-plateau for 1–2 s (phase (iii)). The last phase (iv) occurs after 8 s with a slow decrease (Figure 3b). This complex behavior is rather unexpected, considering the heterogeneous ECL mechanism operating in this experimental configuration with the immobilized labels on nonconductive beads. Since ECL is triggered by an initial electrochemical step, we recorded the chronoamperometric current (Figure S4) during the imposition of the anodic pulse

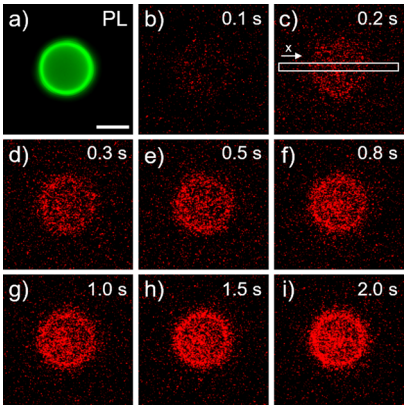

Figure 2. Dynamic recording of ECL mean intensity from a single $[Ru(bpy)_3]^{2+}$-decorated bead in the top-view configuration. (a) PL and (b–i) ECL images of a single labeled bead at different time points during the ECL process. Exposure time for each frame was 100 ms. The rectangle presents the region of interest where the ECL intensity profiles were extracted for Figure 3c. ECL was generated by imposing a constant potential of 1.4 V on a GC electrode in a PBS solution containing 100 mM TPA (pH 7.4). Scale bar: 10 μm.

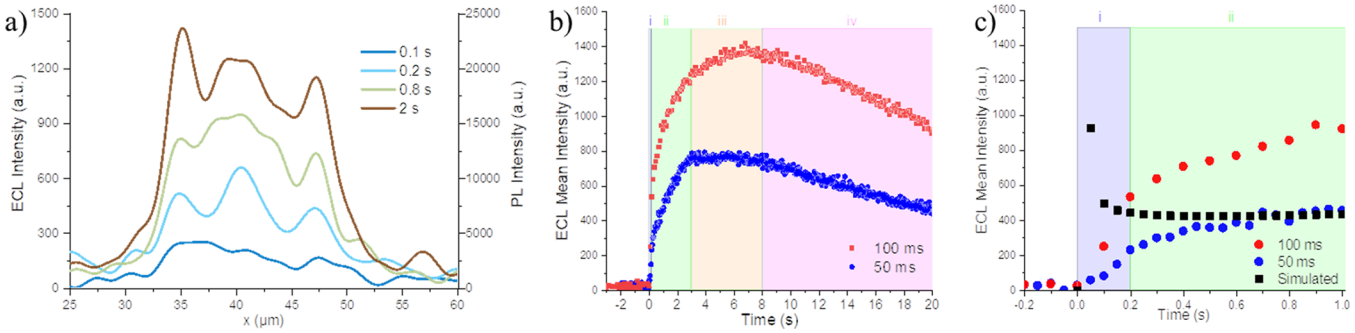

Figure 3. (a) Dynamic analysis of the ECL intensity profiles extracted along the *x*-axis. (b, c) Comparison of the time evolution of the ECL mean intensity from a single $[Ru(bpy)_3]^{2+}$-decorated bead in the top-view configuration with an exposure time of the EMCCD of 50 ms (blue dots) and 100 ms (red dots) with simulated data (black squares) considering the heterogeneous mechanism (vide infra). Same experimental conditions as in Figure 2.

(1.4 V) used to capture the sequence of ECL images (Figure 2b–i). The current decreases monotonically over 20 s. The monotonic decrease of the current does not allow the interpretation of the observed evolution of the ECL signal.

To analyze further the ECL behavior, we considered that the ECL mechanism for the emission of bead-immobilized $[Ru(bpy)_3]^{2+}$ labels follows the simplest heterogeneous pathway (also called the "revisited" route) shown in Scheme 1.[8,48]

Scheme 1. Heterogeneous $[Ru(bpy)_3]^{2+}$ and TPA Coreactant ECL Mechanism[8,48]

(1) $TPAH^+ \rightleftharpoons TPA + H^+$

(2) $TPA - e^- \rightarrow TPA^{\bullet+}$

(3) $TPA^{\bullet+} \rightarrow TPA^{\bullet} + H^+$

(4) $TPA^{\bullet} - e^- \rightarrow$ other products

(5) $[Ru(bpy)_3]^{2+} + TPA^{\bullet} \rightarrow [Ru(bpy)_3]^{+} +$ other products

(6) $[Ru(bpy)_3]^{+} + TPA^{\bullet+} \rightarrow [Ru(bpy)_3]^{2+*} + TPA$

(7) $[Ru(bpy)_3]^{2+*} \rightarrow [Ru(bpy)_3]^{2+} + h\nu$

In this heterogeneous pathway, $[Ru(bpy)_3]^{2+}$ is immobilized on the insulating PS bead (12 μm diameter), and a negligible fraction of the labels is within the direct electron tunneling distance (~1–2 nm). In other words, an infinitesimal fraction of the $[Ru(bpy)_3]^{2+}$ label can be directly oxidized at the electrode surface. Therefore, we can consider that the coreactant is the only species directly oxidized at the electrode surface when imposing 1.4 V. This oxidation produces the cation $TPA^{\cdot+}$ radical (reaction 2) that later deprotonates rapidly (reaction 3) and forms the neutral TPA· radical, which is a highly reducing species. The TPA· radicals reduce the immobilized $[Ru(bpy)_3]^{2+}$ label to the $[Ru(bpy)_3]^{+}$ state (reaction 5). Finally, $[Ru(bpy)_3]^{+}$ reacts with the cation $TPA^{\cdot+}$ radical in the solution phase producing the surface-immobilized excited $[Ru(bpy)_3]^{2+*}$ state (reaction 6) of the label that generates ECL emission (reaction 7). The TPA coreactant is the only diffusing species in this route, and its electrogenerated radicals react with the immobilized labels. In brief, the reactivity of the cation $TPA^{\cdot+}$ radical governs mainly the heterogeneous ECL pathway. Its deprotonation is a fast process, with an estimated rate constant of 2920 s^{-1} corresponding to a half-life time of ~0.24 ms. This short half-life time cannot explain the duration of the initial phases (i) or/and (ii) of the ECL process. In addition, we can estimate the time necessary for the electrogenerated species (i.e., TPA radicals) to diffuse from the electrode surface to the top of the bead, without, in a first order approximation, considering their intrinsic reactivity. We can reasonably assume that all the TPA species have a similar diffusion coefficient, i.e., $D = 5 \times 10^{-6}$ cm^2 s^{-1} in water.[48] The diameter of the beads (12 μm) translates into a diffusion time of ~90 ms necessary for the TPA radicals to reach the top of the bead again without taking into account their chemical reactivity. It is approximately 2 times shorter than the duration of phase i (Figure 3c). This time is even shorter (Figure 3c) if we consider the results of simulations of the ECL mechanism operating at the bead level (vide infra).

To obtain accurate spatial information, we recorded the dynamic ECL behavior of a $[Ru(bpy)_3]^{2+}$-labeled bead under an orthogonal side-view configuration (Figure 1b). Figure 4a shows a set of images. In the PL image (left, green), the upper part is the real physical location of the bead that can help confirm the boundary, while the lower part is the reflection of the bead on the glassy carbon electrode surface. The corresponding ECL images (red) of the bead exhibit that the real light signal comes from ~3 μm from the electrode surface, and the signal at the top is the focused light due to the lens effect of the PS material. Since the signal captured in the side view is limited, the ECL intensity is weaker than that from the top view. Hence, the single-frame exposure time is increased to 300 ms for the sake of image quality. The ECL profile of the bead along the *z*-axis was extracted (Figure S2b). By positioning the peak value of the profile, we measured the height of the maximum ECL emission ($h_{Max\text{-}ECL}$) (Figure 5c). One can observe that at the initial stage of the reaction, the maximum intensity and $h_{Max\text{-}ECL}$ vary with time (Figure 4b). It indicates that the excitation rate of $[Ru(bpy)_3]^{2+}$ changes over time, which may be related to the variation of the deprotonation rate of the TPA cation radical or to the chemical reactivity of the electrode surface.

In an attempt to explain the kinetics of the heterogeneous ECL process, we used numerical digital simulation to model the kinetics of the ECL signal generated at the level of the functionalized beads (see Tables S1–S5 and Figures S5–S10, Supporting Information for details). Finite element simulation is a powerful tool to analyze the concentration profile and the ECL distribution.[54,55] According to the reaction mechanism (Scheme 1), the generation of the luminophore excited state requires the presence of both the strong reducing radical TPrA· and the strong oxidizing radical cation $TPrA^{\cdot+}$ generated from

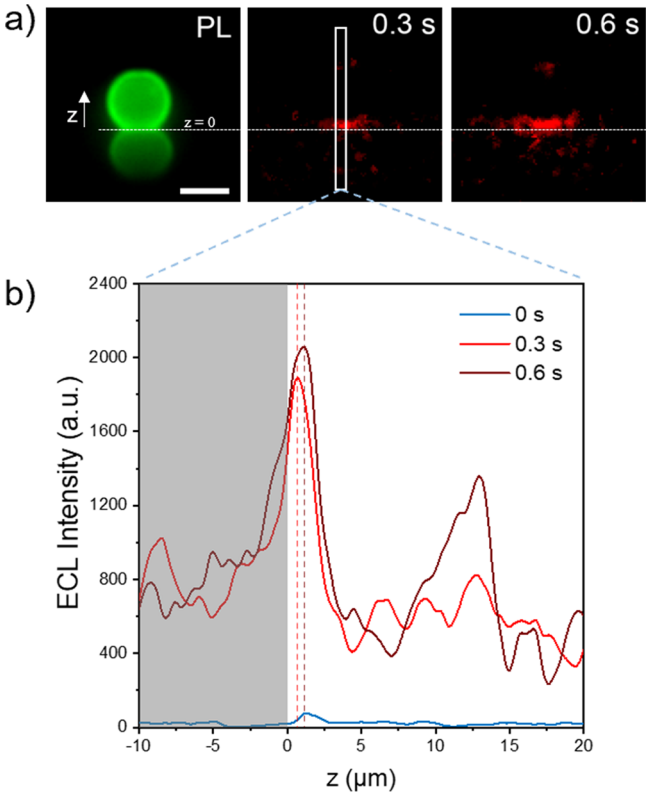

Figure 4. (a) PL (green color) and ECL (red color) images of the same single $[Ru(bpy)_3]^{2+}$-labeled bead in the side-view configuration during the ECL process. The rectangle presents the ROI where the (b) ECL profiles were extracted. The dotted lines indicate the peaks of the ECL profiles. ECL was generated by imposing a constant potential of 1.4 V with a GC electrode in a PBS solution containing 100 mM TPA (pH 7.4). Exposure time for each ECL image: 300 ms. Scale bar: 10 μm.

the electrode surface. These concentration profiles reach a steady state, and with this the ECL intensity, within the first second of the electrochemical stimulation (Videos S2 and S3). Figure 5a,b presents the simulated ECL mapping at t = 1 s from the top view and side view, respectively. It could be seen that the emission layer is annularly distributed at the bottom of the bead with intensity gradients. Such gradients are not obvious in the experimental ECL images, due to the overlay of lights. In the simulation, h_{ECL} and $h_{Max\text{-}ECL}$ reached a plateau at t = 0.2 and t = 0.01 s, respectively, while in the experiments, h_{ECL} and $h_{Max\text{-}ECL}$ peaked around t = 0.8 and t = 0.6 s (Figure 5c). In general, the value of h_{ECL} reflects the kinetic rate of $TPA^{\cdot+}$ deprotonation, and the position of $h_{Max\text{-}ECL}$ depends on the equilibrium concentration of $TPA^{\cdot+}$ and $TPA^{\cdot}$.[49,56] In the simulation, both h_{ECL} and $h_{Max\text{-}ECL}$ remain constant soon after the initial increase.

Under the simulated conditions, the extremely large oxidation rate of TPA at the very beginning results in a burst of ECL intensity at t = 0.05 s and then quickly falls back and stabilizes at a certain value (Figure 3c). Nevertheless, in the actual experiments, ECL signal continued to climb several seconds when the potential was applied. The observed difference between the experimental data and the simulation may be explained by the evolution of the GC surface toward the oxidation of TPA, as reported previously during successive anodic pulses.[53] Another hypothesis is related to the experimental configuration used to record the ECL images. Indeed, for the simulation, bulk conditions (i.e., infinite volume of the solution above the bead) are used, whereas, for ECL imaging, it corresponds more to a thin layer cell because there is a glass coverslip between the microscope objective and the electrode surface with the beads. Whatever, these results demonstrate the unique advantages of dynamic ECL imaging in revealing the kinetics of the ECL process. In the future, this method should be able to provide a variety of dynamic messages for more ECL systems under different conditions and help us to understand the ECL mechanism and reveal transient information.

CONCLUSIONS

In this work, we recorded the time evolution of the bead-based ECL process. Dynamic information such as the behavior of instantaneous ECL intensity, the height of the ECL layer, and the location of maximum ECL emission over time is displayed, which was not achieved by previous static imaging. Based on the parameters obtained above, the kinetics of the coreactant and luminophore during the ECL reactivity was studied. In comparison to simulation, the factors affecting the ECL behavior in experimental conditions were found, which provide a reference for the optimization of the existing bead-based ECL

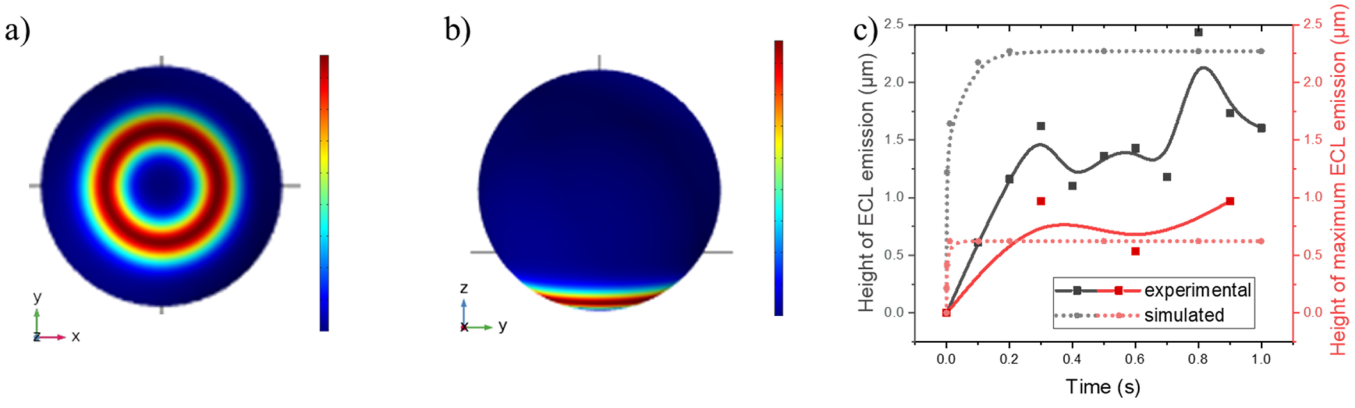

Figure 5. Simulated mapping of the generated $[Ru(bpy)_3]^{2+*}$ excited state (i.e., ECL intensity) at the surface of a 12 μm bead in top- (a) and side-view (b) configurations at t = 1 s after the anodic potential pulse. (c) Evolution of the height of ECL emission (h_{ECL}) over time of the simulation (black circles) and the experimental data (black squares) as well as the height of maximum ECL emission ($h_{Max\text{-}ECL}$) in the simulation (red circles) and the experiment (red squares) of a 12 μm bead.

immunoassays. Differences between the experimental results and the simulation were observed at short times and, even if further surface studies are required, they could be related to the evolution of the GC surface toward the oxidation of TPA.[53] Finally, the dynamic ECL imaging approach is expected to help with more kinetic studies of ECL systems and new reaction mechanisms.

■ ASSOCIATED CONTENT

Supporting Information

The Supporting Information is available free of charge at https://pubs.acs.org/doi/10.1021/acs.analchem.3c02960.

Simulations; ECL data; and chronoamperometric current (PDF)

Top-view ECL microscopy of a single bead recorded when imposing a constant potential of 1.4 V at t = 1 s (dashed blue line) to a GC electrode in a PBS solution containing 100 mM TPA (pH 7.4) (AVI)

Simulation of the ECL signal emitted by a single bead in the side-view configuration (AVI)

Simulation of the ECL signal emitted by a single bead in the top-view configuration (AVI)

■ AUTHOR INFORMATION

Corresponding Authors

Dechen Jiang − *State Key Laboratory of Analytical Chemistry for Life Science and School of Chemistry and Chemical Engineering, Nanjing University, Nanjing, Jiangsu 210023, China;* orcid.org/0000-0002-2845-3621; Email: dechenjiang@nju.edu.cn

Neso Sojic − *CNRS, Bordeaux INP, ISM, UMR 5255, ENSCBP, Univ. Bordeaux, Pessac 33607, France;* orcid.org/0000-0001-5144-1015; Email: sojic@u-bordeaux.fr

Authors

Dongni Han − *CNRS, Bordeaux INP, ISM, UMR 5255, ENSCBP, Univ. Bordeaux, Pessac 33607, France; School of Pharmacy, Nanjing Medical University, Nanjing, Jiangsu 211126, China*

Danjun Fang − *School of Pharmacy, Nanjing Medical University, Nanjing, Jiangsu 211126, China;* orcid.org/0000-0001-5515-3731

Giovanni Valenti − *Department of Chemistry "G. Ciamician", University of Bologna, Bologna 40126, Italy;* orcid.org/0000-0002-6223-2072

Francesco Paolucci − *Department of Chemistry "G. Ciamician", University of Bologna, Bologna 40126, Italy;* orcid.org/0000-0003-4614-8740

Frédéric Kanoufi − *ITODYS, CNRS, Université Paris Cité, Paris F-75013, France;* orcid.org/0000-0002-9784-2380

Complete contact information is available at: https://pubs.acs.org/10.1021/acs.analchem.3c02960

Notes

The authors declare no competing financial interest.

■ ACKNOWLEDGMENTS

This work was supported by Agence Nationale de la Recherche (ELISE—ANR-21-CE42) and the Sino-French International Research Network ELECTROSENS (CNRS).

■ REFERENCES

(1) Liu, Z.; Qi, W.; Xu, G. *Chem. Soc. Rev.* **2015**, *44*, 3117−3142.
(2) Zhang, J.; Arbault, S.; Sojic, N.; Jiang, D. *Annu. Rev. Anal. Chem.* **2019**, *12*, 275−295.
(3) Zanut, A.; Fiorani, A.; Rebeccani, S.; Kesarkar, S.; Valenti, G. *Anal. Bioanal. Chem.* **2019**, *411*, 4375−4382.
(4) Dong, J. L. Y.; Xu, Y.; Chen, F.; Yang, J.; Chen, Y.; Feng, J. *Nature* **2021**, *596*, 244−249.
(5) Ma, C.; Cao, Y.; Gou, X.; Zhu, J.-J. *Anal. Chem.* **2020**, *92*, 431−454.
(6) Fang, Y.; Zhou, Z.; Hou, Y.; Wang, C.; Cao, X.; Liu, S.; Shen, Y.; Zhang, Y. *Anal. Chem.* **2023**, *95*, 6620−6628.
(7) Du, F.; Chen, Y.; Meng, C.; Lou, B.; Zhang, W.; Xu, G. *Curr. Opin. Electrochem.* **2021**, *28*, No. 100725.
(8) Zanut, A.; Fiorani, A.; Canola, S.; Saito, T.; Ziebart, N.; Rapino, S.; Rebeccani, S.; Barbon, A.; Irie, T.; Josel, H. P.; Negri, F.; Marcaccio, M.; Windfuhr, M.; Imai, K.; Valenti, G.; Paolucci, F. *Nat. Commun.* **2020**, *11*, 2668.
(9) Sakanoue, K.; Fiorani, A.; Santo, C. I.; Irkham; Valenti, G.; Paolucci, F.; Einaga, Y. *ACS Sens.* **2022**, *7*, 1145−1155.
(10) Qi, H.; Zhang, C. *Anal. Chem.* **2020**, *92*, 524−534.
(11) Amatore, C.; Pebay, C.; Servant, L.; Sojic, N.; Szunerits, S.; Thouin, L. *ChemPhysChem* **2006**, *7*, 1322−1327.
(12) Chen, M.-M.; Xu, C.-H.; Zhao, W.; Chen, H.-Y.; Xu, J.-J. *J. Am. Chem. Soc.* **2021**, *143*, 18511−18518.
(13) Kanoufi, F.; Sojic, N. *Nature* **2021**, *596*, 194−195.
(14) Rebeccani, S.; Zanut, A.; Santo, C. I.; Valenti, G.; Paolucci, F. *Anal. Chem.* **2022**, *94*, 336−348.
(15) Liu, Y.; Zhang, H.; Li, B.; Liu, J.; Jiang, D.; Liu, B.; Sojic, N. *J. Am. Chem. Soc.* **2021**, *143*, 17910−17914.
(16) Li, B.; Huang, X.; Lu, Y.; Fan, Z.; Li, B.; Jiang, D.; Sojic, N.; Liu, B. *Adv. Sci.* **2022**, *9*, No. e2204715.
(17) Fiorani, A.; Han, D.; Jiang, D.; Fang, D.; Paolucci, F.; Sojic, N.; Valenti, G. *Chem. Sci.* **2020**, *11*, 10496−10500.
(18) Xu, L.; Li, Y.; Wu, S.; Liu, X.; Su, B. *Angew. Chem., Int. Ed.* **2012**, *51*, 8068−8072.
(19) Zhu, M.-J.; Pan, J.-B.; Wu, Z.-Q.; Gao, X.-Y.; Zhao, W.; Xia, X.-H.; Xu, J.-J.; Chen, H.-Y. *Angew. Chem., Int. Ed.* **2018**, *57*, 4010−4014.
(20) Zhu, H.; Jiang, D.; Zhu, J.-J. *Chem. Sci.* **2021**, *12*, 4794−4799.
(21) Han, D.; Goudeau, B.; Lapeyre, V.; Ravaine, V.; Jiang, D.; Fang, D.; Sojic, N. *Biosens. Bioelectron.* **2022**, *216*, No. 114640.
(22) Ma, C.; Wu, S.; Zhou, Y.; Wei, H.-F.; Zhang, J.; Chen, Z.; Zhu, J.-J.; Lin, Y.; Zhu, W. *Angew. Chem., Int. Ed.* **2021**, *60*, 4907−4914.
(23) Chovin, A.; Garrigue, P.; Sojic, N. *Electrochim. Acta* **2004**, *49*, 3751−3757.
(24) Sentic, M.; Virgilio, F.; Zanut, A.; Manojlovic, D.; Arbault, S.; Tormen, M.; Sojic, N.; Ugo, P. *Anal. Bioanal. Chem.* **2016**, *408*, 7085−7094.
(25) Li, H.; Bouffier, L.; Arbault, S.; Kuhn, A.; Hogan, C. F.; Sojic, N. *Electrochem. Commun.* **2017**, *77*, 10−13.
(26) Chovin, A.; Garrigue, P.; Sojic, N. *Electrochim. Acta* **2004**, *49*, 3751−3757.
(27) Guo, W.; Ding, H.; Zhou, P.; Wang, Y.; Su, B. *Angew. Chem., Int. Ed.* **2020**, *59*, 6745−6749.
(28) Zhao, W.; Chen, H.-Y.; Xu, J.-J. *Chem. Sci.* **2021**, *12*, 5720−5736.
(29) Guo, W.; Zhou, P.; Sun, L.; Ding, H.; Su, B. *Angew. Chem., Int. Ed.* **2021**, *60*, 2089−2093.
(30) Ding, H.; Guo, W.; Su, B. *Angew. Chem., Int. Ed.* **2020**, *59*, 449−456.
(31) Ding, H.; Zhou, P.; Fu, W.; Ding, L.; Guo, W.; Su, B. *Angew. Chem., Int. Ed.* **2021**, *60*, 11769−11773.
(32) Ma, Y.; Colin, C.; Descamps, J.; Arbault, S.; Sojic, N. *Angew. Chem., Int. Ed.* **2021**, *60*, 18742−18749.
(33) Glasscott, M. W.; Voci, S.; Kauffmann, P. J.; Chapoval, A. I.; Dick, J. E. *Langmuir* **2021**, *37*, 2907−2912.
(34) Glasscott, M. W.; Dick, J. E. *J. Phys. Chem. Lett.* **2020**, *11*, 4803−4808.

(35) Gou, X.; Xing, Z.; Ma, C.; Zhu, J.-J. *Chem. Biomed. Imaging* **2023**, *1*, 414−433.
(36) Guo, M.; Du, D.; Wang, J.; Ma, Y.; Yang, D.; Haghighatbin, M. A.; Shu, J.; Nie, W.; Zhang, R.; Bian, Z.; Wang, L.; Smith, Z. J.; Cui, H. *Chem. Biomed. Imaging* **2023**, *1*, 179−185.
(37) Dong, J.; Xu, Y.; Zhang, Z.; Feng, J. *Angew. Chem., Int. Ed.* **2022**, *61*, No. e202200187.
(38) Valenti, G.; Scarabino, S.; Goudeau, B.; Lesch, A.; Jović, M.; Villani, E.; Sentic, M.; Rapino, S.; Arbault, S.; Paolucci, F.; Sojic, N. *J. Am. Chem. Soc.* **2017**, *139*, 16830−16837.
(39) Voci, S.; Goudeau, B.; Valenti, G.; Lesch, A.; Jović, M.; Rapino, S.; Paolucci, F.; Arbault, S.; Sojic, N. *J. Am. Chem. Soc.* **2018**, *140*, 14753−14760.
(40) Ma, C.; Wei, H.-F.; Wang, M.-X.; Wu, S.; Chang, Y.-C.; Zhang, J.; Jiang, L.-P.; Zhu, W.; Chen, Z.; Lin, Y. *Nano Lett.* **2020**, *20*, 5008−5016.
(41) Ma, C.; Wu, W.; Li, L.; Wu, S.; Zhang, J.; Chen, Z.; Zhu, J.-J. *Chem. Sci.* **2018**, *9*, 6167−6175.
(42) Wu, K.; Chen, R.; Zhou, Z.; Chen, X.; Lv, Y.; Ma, J.; Shen, Y.; Liu, S.; Zhang, Y. *Angew. Chem., Int. Ed.* **2023**, *62*, No. e202217078.
(43) Kerr, E.; Hayne, D. J.; Soulsby, L. C.; Bawden, J. C.; Blom, S. J.; Doeven, E. H.; Henderson, L. C.; Hogan, C. F.; Francis, P. S. *Chem. Sci.* **2022**, *13*, 469−477.
(44) Haghighatbin, M. A.; Laird, S. E.; Hogan, C. F. *Curr. Opin. Electrochem.* **2018**, *7*, 216−223.
(45) Zanut, A.; Palomba, F.; Rossi Scota, M.; Rebeccani, S.; Marcaccio, M.; Genovese, D.; Rampazzo, E.; Valenti, G.; Paolucci, F.; Prodi, L. *Angew. Chem., Int. Ed.* **2020**, *59*, 21858−21863.
(46) Rebeccani, S.; Wetzl, C.; Zamolo, V. A.; Criado, A.; Valenti, G.; Paolucci, F.; Prato, M. *Chem. Commun.* **2021**, *57*, 9672−9675.
(47) Deiss, F.; LaFratta, C. N.; Symer, M.; Blicharz, T. M.; Sojic, N.; Walt, D. R. *J. Am. Chem. Soc.* **2009**, *131*, 6088−6089.
(48) Miao, W.; Choi, J. P.; Bard, A. J. *J. Am. Chem. Soc.* **2002**, *124*, 14478−14485.
(49) Sentic, M.; Milutinovic, M.; Kanoufi, F.; Manojlovic, D.; Arbault, S.; Sojic, N. *Chem. Sci.* **2014**, *5*, 2568−2572.
(50) Sojic, N. *Analytical Electrogenerated Chemiluminescence: From Fundamentals to Bioassays*; Royal Society of Chemistry, 2019.
(51) Wang, Y.; Ding, J.; Zhou, P.; Liu, J.; Qiao, Z.; Yu, K.; Jiang, J.; Su, B. *Angew. Chem., Int. Ed.* **2023**, *62*, No. e202216525, DOI: 10.1002/anie.202216525.
(52) Dutta, P.; Han, D.; Goudeau, B.; Jiang, D.; Fang, D.; Sojic, N. *Biosens. Bioelectron.* **2020**, *165*, No. 112372.
(53) Han, D.; Goudeau, B.; Jiang, D.; Fang, D.; Sojic, N. *Anal. Chem.* **2021**, *93*, 1652−1657.
(54) Daviddi, E.; Oleinick, A.; Svir, I.; Valenti, G.; Paolucci, F.; Amatore, C. *ChemElectroChem.* **2017**, *4*, 1719−1730.
(55) Imai, K.; Valenti, G.; Villani, E.; Rapino, S.; Rampazzo, E.; Marcaccio, M.; Prodi, L.; Paolucci, F. *J. Phys. Chem. C* **2015**, *119*, 26111−26118.
(56) Fiorani, A.; Han, D.; Jiang, D.; Fang, D.; Paolucci, F.; Sojic, N.; Valenti, G. *Chem. Sci.* **2020**, *11*, 10496.